



# **Numerical Investigation of Magnetic Field Effects on Dusty Plasma Crystals**

**Project code: PLAS-Coppins-1**

**00948696**

Supervisor: Dr. M. Coppins

Assessor: Dr. M. Galand

Department of Physics

Imperial College London

This report is submitted for the degree of

*MSci in Physics*

Word Count: 9978

April 2018



## **Abstract**

Micro-sized charged particles, when suspended in low-temperature glow discharges, are known to spontaneously form a hexagonal crystal lattice. If a vertical magnetic field is applied, the crystal will rotate and occasionally, regions devoid of particles, termed voids, are formed. These behaviours are largely dependent on the strength and geometry of the magnetic field. The magnitude of the ion-drag force and the origin of void formations in such experiments have not yet been properly theoretically, nor numerically studied. In this project we have developed a numerical model that analyses the forces on mono-dispersed, spherical, micro-sized particles (used to represent dust particles in real life scenarios) as they are released into a glow discharge. For the first time, it provides a correction to the existing theory for the ion drift velocities in a magnetic field and is numerically verified. It also numerically investigates, for the first time, the origin of void formation in the presence of a magnetic field. We will simulate the physics of two literature experiments from start to finish — from crystal formation in the absence of a magnetic field, to dust rotation and void formation due to a magnetic dipole. We conclude that the simulation is successful in capturing the important physics found in real experimental results. However, several discrepancies between simulation and literature, such as void size, are identified, and improvements are proposed. Nevertheless, the framework created in this project lays out the foundations for further research.



# Table of contents

<b>1</b>	<b>Introduction</b>	<b>1</b>
1.1	Dusty Plasmas . . . . .	1
1.2	Previous relevant work . . . . .	1
1.2.1	Crystal formation . . . . .	1
1.2.2	Magnetic field effects . . . . .	2
1.3	Motivation and Broader scope . . . . .	4
1.4	Project goals . . . . .	5
<b>2</b>	<b>Theory</b>	<b>7</b>
2.1	Basic plasma physics . . . . .	7
2.2	Electrostatic sheath . . . . .	8
2.3	Dust Grain Interactions . . . . .	9
2.3.1	Orbital Motion Limited Theory . . . . .	9
2.4	Magnetic field effects . . . . .	12
2.4.1	Ion Drag Force . . . . .	12
2.4.2	Ion-Neutral Collisions . . . . .	15
2.4.3	Neutral Drag Force . . . . .	17
2.4.4	Void Formation . . . . .	17
2.4.5	Summary . . . . .	20

<b>3 Numerical Method</b>	<b>21</b>
3.1 Plasma Sheath and Crystal Formation . . . . .	21
3.2 Magnetic Dipole . . . . .	23
3.3 Drag forces & Dust Rotation . . . . .	24
3.3.1 Ion-Neutral Collision Correction Factor . . . . .	24
3.3.2 Curvature and Grad-B ion drifts . . . . .	25
3.3.3 Internal Electric Field Modification . . . . .	25
3.3.4 Summary . . . . .	26
<b>4 Results</b>	<b>29</b>
4.1 Crystal Structure . . . . .	29
4.2 Magnetic Field Effects . . . . .	30
4.2.1 Ion-Neutral Collision . . . . .	30
4.2.2 Void formation . . . . .	31
4.2.3 Crystal Rotation . . . . .	32
<b>5 Discussion</b>	<b>39</b>
5.1 Comparisons with literature . . . . .	39
5.1.1 Plasma Crystal Structure . . . . .	40
5.1.2 Saitou's experiment . . . . .	41
5.1.3 Konopka et al's experiment . . . . .	43
5.2 Improvements to the model . . . . .	45
<b>6 Conclusion</b>	<b>47</b>
<b>References</b>	<b>53</b>

# **Chapter 1**

## **Introduction**

### **1.1 Dusty Plasmas**

Plasmas are collectively neutral, ionised gases, comprised of freely moving ions and electrons. A dusty plasma is formed when solid particles (usually dust grains) of sizes ranging from several nanometers to several micrometres are suspended within a plasma. Under simple laboratory conditions, such plasmas can be generated through the ionisation of a neutral gas, by an externally applied electric field in a process called electric discharge [1]. Dusty plasmas are often enclosed in containers, where a range of interesting phenomena occur, between the boundary of the plasma and the confining walls.

### **1.2 Previous relevant work**

#### **1.2.1 Crystal formation**

Once inserted into the plasma, dust grains become negatively charged and repel each other. When the inter-grain potential exceeds their kinetic energies, the dust grains spontaneously arrange themselves to form hexagonal lattices called Coulomb crystals or dusty plasma crystals

(See fig. 1.1). This crystallisation process was first observed by Thomas et al [2]. In this experiment, called RF discharge, an argon plasma was created by applying an alternating current with radio-frequency between two electrodes.

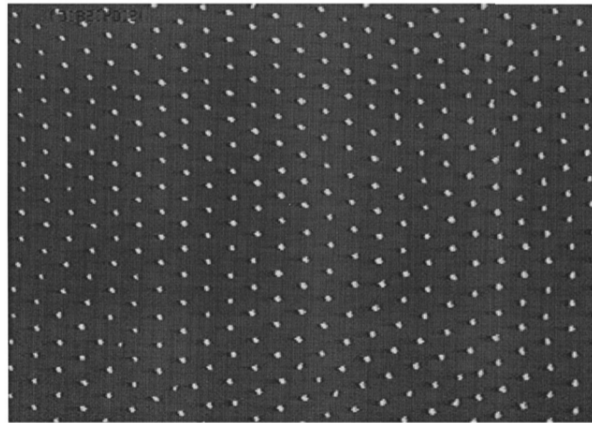


Figure 1.1: Experimental crystal formation from the RF discharge experiment performed by Thomas et al [3]. This shows a hexagonal lattice structure where most dust grains are surrounded by six others.

### 1.2.2 Magnetic field effects

Konopka et al. performed an experiment with a similar setup (fig. 1.2) and observed that dusty plasma crystals rotate under the presence of an approximately vertical magnetic field [4]. Simultaneously, dust grains were also expelled from the crystal centre, forming a void (fig. 1.3).

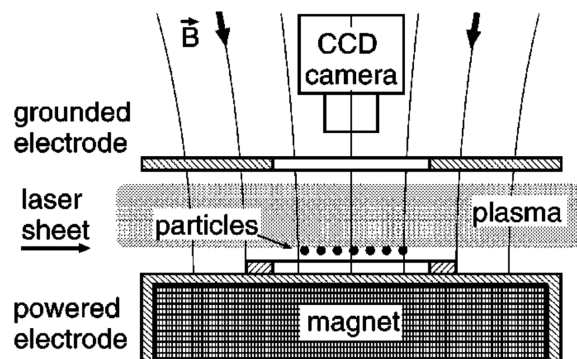


Figure 1.2: Konopka's experimental setup [4]. Argon discharge plasma is suspended between two electrodes and a vertical magnetic field is applied. Monodisperse micro-sized particles are dropped into the plasma and their motions are recorded by a CCD camera.

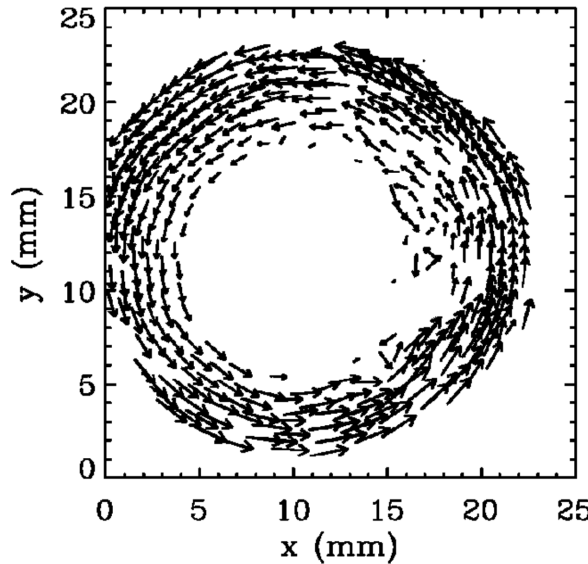


Figure 1.3: Konopka's experiment showing a dusty plasma crystal rotating counter-clockwise (direction is shown by the arrows), influenced by an external magnetic field perpendicular to the figure's plane. A void is formed in the centre [4].

Another experiment, performed by Saitou [5], used a smaller magnet to generate a non-uniform magnetic field inside the plasma. The magnetic field profile is shown in fig. 1.4. This is very important in the resulting dust behaviour, as we will see in Chapter 4.

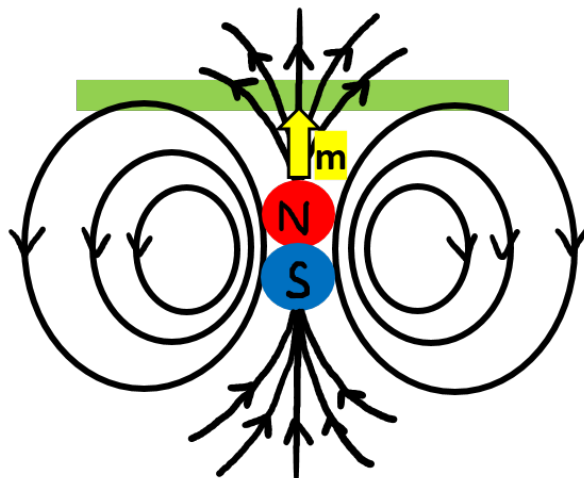


Figure 1.4: Qualitative profile of the magnetic field lines of a magnetic dipole (not to scale). The green horizontal rectangle on the top of the dipole represents the equilibrium position of the dusty plasma crystal. Different sections of the crystal are subject to magnetic field lines pointing in different directions. The  $\mathbf{m}$  vector represents the direction of the magnetic moment [6].

Several interesting pieces of physics were identified in the two RF discharge experiments:

1. A void is formed in both experiments despite the different magnetic field geometries.
2. The motion of dust grains were approximately circular but followed zigzag patterns with no predictable frequencies.
3. A low applied voltage results in a holistic rotation of the crystal without any shear between the grains. This was called ‘rigid rotation’. By increasing the applied voltage, a transition in the dust grain rotational behaviour eventually emerged, where the angular velocities developed a radial dependence. Grains closer to the crystal centre rotated with larger angular speeds than those at larger radii. This was termed ‘differential rotation’.

There have not yet been proper theoretical and numerical investigations into the cause of void formations in dusty plasma crystals. Their origins have been qualitatively attributed to a change in the internal electric field inside the plasma [4].

Recently, a theoretical study of the plasma behaviour under a magnetic dipole influence was done in 2018 by J. Gibson [7]. He developed a novel method of calculating the number density distribution of the charged particles in the plasma, by studying the kinetics of electron motion. He concluded that there are regions inside the plasma where electrons cannot access, as they are deflected too strongly by the magnetic field. This means that the magnetic field causes a change in the spatial distribution of charge inside the plasma, which can in turn influence the motion of dust grains.

### 1.3 Motivation and Broader scope

Although the dusty plasma crystallisation process is usually observed under specific laboratory settings, the physics of such charged micro-sized particles can be very informative when inspecting the various other fields that dusty plasmas are relevant in. The initial interest in dusty

plasmas was generated due to their presence in astrophysics and atmospheric physics; within comets, interstellar media to name a few [1]. A famous example is that the spokes observed in Saturn's rings arise from dust particles levitating in dense plasmas, which are in turn produced from meteor collisions [8]. Dusty plasmas also exist at the edges of tokamaks (fusion reactors), surrounded by huge magnetic fields [9]. Furthermore, understanding the behaviour of dusty plasmas are of great importance in the fabrication and miniaturisation of microelectronics [10]. Thus, deeper insights into the role of magnetic fields in dusty plasma *crystals* can be very helpful when trying to better comprehend the role of dusty plasmas, which exist ubiquitously throughout the aforementioned areas.

## 1.4 Project goals

This project aims to theoretically study, then numerically simulate the behaviour of dusty plasma crystals exposed to magnetic fields. It intends to investigate the phenomena of crystal rotation and the origins of void formation. It will then compare the simulations with literature experiments to see if the physics has been correctly captured. More specifically, Chapter 2 delves into the theory behind crystal formation and the effects of magnetic fields. Chapter 3 focuses on numerical methods and implementation, whose results are examined in Chapter 4. Chapter 5 compares simulations with literature, discusses improvements to be made and identifies potential avenues for further research. Finally, conclusions are drawn in Chapter 6.

There are several novel components offered by the project. Firstly, modifications to the known theory of ion drift velocities are made, which we also aim to numerically verify. Secondly, inspired by Gibson's theories, we wish to simulate a change in the internal electric field of the plasma in the attempt to observe void formations. Thus, for the first time, this project aspires to numerically demonstrate both crystal rotation and void formation that effectively captures existing experimental findings.



# Chapter 2

## Theory

In this section, we will look into the theory of how plasmas behave when they are confined. Then, we discuss the behaviour of dust grains in such environments and the effects of magnetic fields.

### 2.1 Basic plasma physics

The plasma's ion temperature is normally comparable to room temperature ( $\approx 0.03\text{eV}$ ), while the electron temperature is typically a hundred times larger [11]. This is because incoming energy from the RF waves more effectively couple to electrons, causing them to have higher thermal energies, and initiate ionisation through collisions with neutral atoms. The plasma is assumed to be collectively neutral, and the electron and ion number density equal,  $n_e = n_i$  (quasi-neutral condition) [12]. This is because any departures from neutrality will generate a large internal electric field, and electrons (the lightest of the plasma particles) will move quickly to neutralise it.

A charged object in a plasma will become surrounded by the oppositely charged particle species. This phenomenon, called Debye shielding [13], alters the objects' apparent potential. The characteristic length scale over which the potential drop rapidly occurs is called the Debye

length. This is a key parameter that is used throughout the report as it is a unit of length that many things are compared against. In a dusty plasma, the dusty Debye length is

$$\lambda_D = \frac{\lambda_{De}\lambda_{Di}}{\sqrt{\lambda_{De}^2 + \lambda_{Di}^2}}, \quad (2.1)$$

where  $\lambda_{Dn} = \sqrt{\frac{k_B T_n}{4\pi n_{n0} e^2}}$  is the Debye length of the species  $n \in \{i = \text{ions}, e = \text{electrons}\}$  [14]. Here,  $k_B$  is Boltzmanns constant,  $T_n$  is the temperature of species  $n$ ,  $n_{n0}$  is the background number density of species  $n$ , and  $e$  is the electron charge. The plasma parameters used in our simulations are on the same order of magnitude as those used by Konopka and Saitou, namely  $n_e = n_i \sim 10^{15} \text{ m}^{-3}$ ,  $T_e \sim 4 \text{ eV}$  (electron temperature), and  $T_i \sim 310 \text{ K}$  (ion temperature).

## 2.2 Electrostatic sheath

Inside the cylinder confining our plasma, the region of interest is near boundary walls (more specifically, this is the lower electrode used in experiments). When plasmas come into contact with a surface, a positively charged spatial region called the sheath is formed, with a length scale that is typically a few  $\lambda_D$ s across. Dust particles fall under gravity and eventually levitate above the bottom electrode, which repels negative objects. To see why this is, we begin by studying the relevant physics of the sheath.

Recall that electrons have a larger thermal velocity than ions. This means that they collide and become captured more frequently with the walls, causing them to become net negatively charged. In order to calculate the final wall potential, consider the condition where there are no external current/electric fields. When the system settles into equilibrium, the net electron and ion flux ( $I_e$  and  $I_i$ ) are equal. Electron flux is caused by their fast, thermal motion. On the other hand, ions enter the sheath with a large velocity, because they are accelerated by the electric field from the negative wall potential. This occurs in a region before the sheath (called the

pre-sheath [15]) and results in the ion flux. The flux magnitudes are

$$I_e = en_0 \sqrt{\frac{k_B T_e}{2\pi m_e}} e^{\frac{e\phi}{k_B T_e}}, \quad (2.2)$$

$$I_i = \sqrt{en_0} \sqrt{\frac{k_B T_e}{m_i}}, \quad (2.3)$$

where  $m_e$  and  $m_i$  are the electron and ion (argon) mass respectively [16]. The background number density,  $n_0$ , is equal for electrons and ions from a singly ionised gas (quasi-neutrality). By using the condition of flux equality at equilibrium, the solution for  $\phi$ ,

$$\phi = \frac{k_B T_e}{2e} \left[ \ln \left( \frac{2\pi m_e}{m_i} \right) - 1 \right], \quad (2.4)$$

is called the floating potential. This is the potential difference between the wall and the plasma. It is important because it sets up an electric field inside the sheath, which provides one of the dominant forces acting on the dust grains.

## 2.3 Dust Grain Interactions

We would now like to understand what happens when dust grains are introduced to the confined plasma.

### 2.3.1 Orbital Motion Limited Theory

To figure out the surface potential of a dust grain at equilibrium, we employ the widely accepted Orbital Motion Limited theory (OML) to calculate the charging currents caused by the collection of electrons and ions onto the dust surface [17] (see fig. 2.1).

This theory considers the trajectories of charged particles as they intersect with the dust grain. If they directly hit or just graze the dust grain, they are absorbed and their charges

donated. Previously, we attributed the negative potential of the walls to the high electron collisional frequency. The same reasoning can be applied to dust grains.

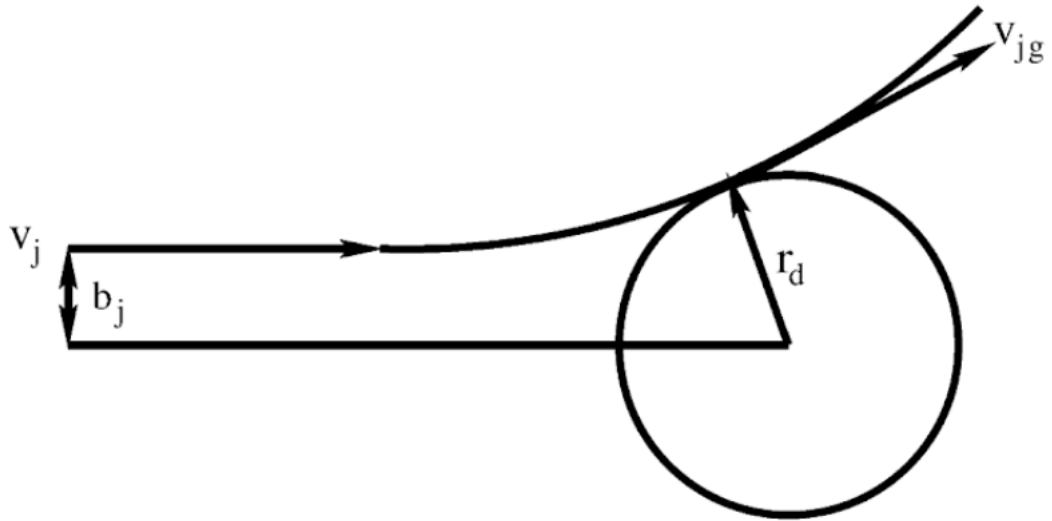


Figure 2.1: Sketch of a charged particle's trajectory as it grazes a dust particle with radius  $r_d$ . The charged particle has initial velocity  $\mathbf{v}_j$ , final velocity  $\mathbf{v}_{jg}$  and impact parameter  $b_j$  [14].

Assuming that the plasma species follow a Maxwellian velocity distribution [18], the ion charging current is calculated by employing energy and angular momentum conservations,

$$I_i = 4\pi r_d^2 n_0 e \sqrt{\frac{k_B T_i}{2\pi m_i}} \left( 1 - \frac{e\phi_d}{k_B T_i} \right), \quad (2.5)$$

where  $\phi_d$  is the dust grain surface potential [14]. The number density of electrons in the plasma follow the Boltzmann distribution, i.e.  $n_e = n_0 e^{\frac{e\phi}{k_B T_e}}$  [19]. This results in the electron charging current

$$I_e = -4\pi r_d^2 e n_0 \sqrt{\frac{k_B T_e}{2\pi m_e}} e^{\frac{e\phi_d}{k_B T_e}}. \quad (2.6)$$

At steady state, the net charging current (eq. (2.5) + eq. (2.6)) must be zero. This results in

$$\sqrt{\frac{m_e T_i}{m_i T_e}} \left( 1 - \frac{e\phi_d}{k_B T_i} \right) - e^{\frac{e\phi_d}{k_B T_e}} = 0, \quad (2.7)$$

which can be solved to obtain the dust surface potential  $\phi_d$ . This is important as it allows us to calculate the surface charge,

$$Z_d = \frac{4\pi\epsilon_0 r_d}{e}, \quad (2.8)$$

accumulated on the dust grain. Thus, we can obtain the potential profile of the dust grains and simulate their inter-grain repulsions. This potential is the Debye-Hückel potential [20],

$$\phi(r) = \frac{\phi_d r_d}{r} e^{\frac{r-r_0}{\lambda_D}}, \quad (2.9)$$

which includes the  $r^{-1}$  factor that resembles the Coulomb potential, but also contains an exponential drop-off term that originates from plasma screening/shielding.

There are other phenomena contributing to the final charge on the dust grain. For example, collisions from high energy electrons can cause further, secondary electron emissions [21]. Electrons can also quantum tunnel through the dust grain potential barrier, releasing energy that can cause further electron excitations and emissions [22]. These additional effects are not included as they are negligible compared to the primary charging process accounted for in OML.

The OML theory is valid for dust grains of radius  $r_d$  much smaller than the Debye length,  $\lambda_D$ . The Debye length for our simulated plasma is on the order of  $10^{-4}$  m, while the experimental dust radius used by Konopka (and our simulation) is on the order of  $10^{-6}$  m. As this requirement is satisfied, we will use OML to determine the charge and potential of our simulated dust grains.

In summary, a negative potential (relative to the plasma) is created at the cylinder walls. This results in an internal electric field that is strongest in the sheath and extends itself into the plasma. Positive ions are accelerated towards the walls, while electrons are deflected. The electric field counteracts the gravitational pull on the dust grains, causing them to attain a stable equilibrium inside the sheath. The simulation employs a radially symmetric cylinder, so the

electric field generated by the walls points radially outwards, and pushes dust grains (which are negatively charged) towards the centre.

Before any magnetic fields are introduced, the simulation should reproduce the crystal structure seen in fig. 1.1. This crystal can be characterised by the Coulomb coupling parameter [23],

$$\Gamma = \frac{(Z_d e)^2}{4\pi\epsilon r_d k_B T} e^{\frac{r_d}{\lambda_D}} \quad (2.10)$$

which is the ratio between dust grains' interaction potential energies and their kinetic energies. Crystal formation occurs when  $\Gamma \gg 1$ .

## 2.4 Magnetic field effects

We now introduce a magnetic dipole beneath the cylinder at the radial coordinate,  $r = 0$ . This section focuses on the effects of the dipole's magnetic field on the dusty plasma.

### 2.4.1 Ion Drag Force

A magnetic field causes charged particles of mass  $m$  and charge  $q$  to move in circular orbits with a gyration frequency of  $\omega = \frac{qB}{m}$ . In Konopka's experiment (see fig. 1.2), a magnet is placed below the bottom electrode and the magnetic field is approximately vertical at all points in the sheath. In the simulation, a magnetic dipole is used to represent the idealised case of a vanishingly small bar magnet. This allows us to study a more complex and interesting scenario, where the magnetic field is not spatially uniform.

If charged dust grains are moving in such a magnetic field, they will be subject to the usual Lorentz force  $\mathbf{F} = eZ_d \mathbf{v} \times \mathbf{B}$ . However, the dominant force on the dust grains actually come from drag forces caused by charged plasma particles.

When an electric field is also present, it exerts a force on charged particles along the field lines. As these particles' speeds change, so does the magnetic force, and thus gyro-radius. The

result is a drift motion in the direction of the  $\mathbf{E} \times \mathbf{B}$  vector, called the  $\mathbf{E} \times \mathbf{B}$  ion drift velocity. This is given by

$$\mathbf{v}_{E \times B} = \frac{\mathbf{E} \times \mathbf{B}}{|\mathbf{B}|^2}. \quad (2.11)$$

This is the dominant effect caused by the two fields [24]. Notice that it is independent of charge, which means ions and electrons both drift in the same direction. The physical picture described here is that on average, charged particles are gyrating around a guiding centre, which drifts with velocity  $\mathbf{v}_{E \times B}$ . Other sources of charged particle drifts arise due to the non-uniformity of the magnetic field. These are called the grad-B and curvature drifts  $\mathbf{v}_{\text{gradB}}$  and  $\mathbf{v}_{\text{curvature}}$  [24]. They act in the same direction and are collectively given by,

$$\mathbf{v}_{\text{gradB}} + \mathbf{v}_{\text{curvature}} = \frac{m}{qB} \left( v_{\parallel}^2 + \frac{v_{\perp}^2}{2} \right) \frac{\mathbf{B} \times \vec{\nabla}B}{|\mathbf{B}|^2}, \quad (2.12)$$

for a charged particle of mass  $m$  and charge  $q$ .  $v_{\parallel}$  and  $v_{\perp}$  represent the component of the particle's velocity parallel and perpendicular to the magnetic field respectively. The total velocity of particle  $i$ ,  $|\mathbf{v}_{\text{total}}| = \sqrt{v_{\parallel}^2 + v_{\perp}^2}$ , is taken as its thermal speed. Equipartition of energy is used to divide the total velocity amongst components parallel (vertical velocity along Z-axis) and perpendicular (radial velocity in XY-plane) to the magnetic field. The grad-B drift arises due to a gradient in the magnetic field. The instantaneous gyroradius of a charged particle will decrease as it travels from regions of weaker to stronger magnetic fields (and vice versa). As charged particles gyrate, the curvature of the magnetic field lines causes them to experience a centrifugal acceleration outwards, giving rise to the curvature drift. As the electric and magnetic fields only consist of radial and vertical components, the forces arising from the cross products shown in eqs. (2.11) and (2.12) are predominantly in the  $\hat{\theta}$  direction. Hence, the crystal should rotate in the XY-plane.

As electrons are extremely light in comparison to ions, their contributions to the drag force are neglected. Thus the total ion drift velocity caused by combined effects from the magnetic and electric fields is  $\mathbf{v}_{\text{drift}} = \mathbf{v}_{\text{ExB}} + \mathbf{v}_{\text{gradB}} + \mathbf{v}_{\text{curvature}}$ .

As ions and neutrals collide onto the dust surface, the rate of imparted momentum manifests itself into a drag force. There are two approaches to calculate the ion drag. The first is called binary collision approach [25], which considers the ballistic trajectories of ions as they scatter onto the grain. The second method is to solve for the potential around the grain using Poisson's equation [26]. A recently proposed "hybrid" model [27] takes both these methods into account, proposing the following total drag force equation,

$$F_i = \sqrt{2\pi} r_d^2 n_i m_i v_{T_i}^2 \left( \sqrt{\frac{\pi}{2}} \operatorname{erf} \left( \frac{u}{\sqrt{2}} \right) [1 + u^2 + (1 - u^{-2})(1 + 2z \frac{T_e}{T_i}) + 4z^2 \left( \frac{T_e}{T_i} \right)^2 u^{-2} \ln \Lambda] + u^{-1} [1 + 2z \frac{T_e}{T_i} + u^2 - 4z^2 \left( \frac{T_e}{T_i} \right)^2 \ln \Lambda] e^{-\frac{u^2}{2}} \right), \quad (2.13)$$

where  $\ln \Lambda$  is called the Coulomb logarithm, a plasma parameter that describes how much more effective small-angled collisions are compared to large angled collisions [28]. This value ranges from 10-20 for most plasmas and will be taken as 15 for this project, as its exact magnitude in this range will not notably affect the resulting force. The ion thermal velocity is given by  $v_{T_i}$ , while  $u = \frac{v_{\text{drift}}}{v_{T_i}}$ ,  $z = \frac{|Z_d|e^2}{4\pi\epsilon_0 r_d k_B T_e}$  and erf is the error function defined as [29]

$$\operatorname{erf}(x) = \frac{2}{\sqrt{\pi}} \int_0^x e^{-t^2} dt, \text{ for } -\infty < x < \infty. \quad (2.14)$$

The ion drift velocity is a crucial component of this equation as it markedly affects the drag force's order of magnitude. However, a problem becomes apparent when inspecting the drift velocities (see eqs. (2.11) and (2.12)) in the limit of large electric fields and small magnetic fields. Not only will the velocity exceed the speed of light, but will tend towards infinity as the magnetic field vanishes! This issue is discussed and resolved in Section 2.4.2.

### 2.4.2 Ion-Neutral Collisions

We have studied the ion drift velocity caused by the external magnetic field and discovered an issue of diverging drift velocities (eqs. (2.11) and (2.12)). This paradox is resolved when considering the assumptions that the derivations are based on. When the magnetic field is very weak (compared to the electric field), it is no longer able to induce a gyration around a guiding centre. Instead, the ion is merely slightly deflected, and is essentially accelerated only by the electric field.

To solve this issue numerically, we must consider something that greatly affects the drift velocity, but has been neglected so far. This is the collisions between ions and neutral atoms. To see why this phenomenon must be included, let us consider the ion's motion.

The ion gyration period for our plasma parameters is  $\frac{2\pi m_i}{qB} \sim 10^{-4}$  s, which is much larger than the average ion-neutral collision time of  $10^{-8}$  s in an argon plasma [30]. This means that ions will be knocked off their original trajectory before completing a full revolution. To account for this, we must solve the ion's equations of motion and include the effects of collisions with neutrals. According to our setup, the magnetic field of a dipole in cylindrical coordinates has a radial and vertical component,  $B = [B_r, 0, B_z]$ , while the electric field is  $\mathbf{E} = [E_r, 0, E_z]$  due to the sheath. The ion velocity is denoted  $\mathbf{v} = [v_r, v_\theta, v_z]$ . For simplicity, assume the ion starts with thermal motion along the radial axis, i.e.  $\mathbf{v}(t = 0) = [v_T, 0, 0]$ . The cross product  $\mathbf{v} \times \mathbf{B} = [v_\theta B_z, -(v_r B_z - v_z B_r), -B_r v_\theta]$  and the Lorentz equations of motion for the ion are

$$m \frac{dv_r}{dt} = q(E_r + v_\theta B_z), \quad (2.15)$$

$$m \frac{dv_\theta}{dt} = q(B_r v_z - v_r B_z), \quad (2.16)$$

$$m \frac{dv_z}{dt} = q(E_z - v_\theta B_r). \quad (2.17)$$

The cross product  $\mathbf{E} \times \mathbf{B} = [0, B_r E_z - B_z E_r, 0]$  shows that the ion drift velocity is along the  $\hat{\theta}$  direction. This means we can simply focus on eq. (2.16). Taking the second derivative of

eq. (2.16) and plugging in eq. (2.15)) and eq. (2.17)) gives

$$\begin{aligned}\frac{d^2v_\theta}{dt^2} &= -\frac{q^2v_\theta}{m^2}(B_z^2 + B_r^2) - \frac{q^2}{m^2}(E_rB_z - E_zB_r), \\ &= -\omega^2v_\theta - k,\end{aligned}\tag{2.18}$$

where  $\omega = \frac{q^2(B_z^2 + B_r^2)}{m^2} = \frac{q|\mathbf{B}|^2}{m^2}$  simplifies to become the cyclotron frequency squared  $\omega^2$ , where  $k = \frac{q^2}{m^2}(E_rB_z - E_zB_r)$ . Plugging in the ansatz  $v_\theta(t) = A(1 - \cos(\omega t))$  into eq. (2.18) yields

$$v_\theta(t) = \frac{k}{\omega^2}(1 - \cos(\omega t)).\tag{2.19}$$

In general, the mean displacement  $\bar{\lambda}_{\text{drift}}$  covered by the ion in-between collisions with neutrals is given by [31]

$$\bar{\lambda}_{\text{drift}} = \int_0^\infty e^{-\frac{t}{\tau}} \left( \int_0^t \mathbf{v} dt \right) \frac{dt}{\tau},\tag{2.20}$$

with average collision time  $\tau$ . Inserting eq. (2.19) into eq. (2.20) gives

$$\begin{aligned}\bar{v}_{\text{drift}} &= \frac{\bar{\lambda}_{\text{drift}}}{\tau}, \\ &= \int_0^\infty \frac{1}{\tau^2} \left( \int_0^T \frac{k}{\omega^2}(1 - \cos(\omega t)) dt \right) e^{-\frac{T}{\tau}} dT, \\ &= \frac{q^2\tau^2(E_rB_z - E_zB_r)}{m^2(1 + \omega^2\tau^2)}.\end{aligned}\tag{2.21}$$

This is our proposed corrected expression for the ion drift velocity given our specific setup geometry. It no longer diverges to infinity in the limit of small magnetic fields. The interference of neutral atoms in the ion's path means that the true ion drift velocity is significantly smaller than that given by eq. (2.11). This "corrected" ion drift velocity is used in eq. (2.13) to determine the ion drag force imparted on the dust grains. The validity of our theory is tested in Section 3.3.1.

### 2.4.3 Neutral Drag Force

The momentum transfer between dust grains and neutral particles gives rise to the neutral drag force. As the neutrals are originally stationary, the neutral drag force only becomes apparent when the dust grains gain momentum from the ion drag. The drag from neutrals of mass  $m_N$  is proportional to their flux and momentum onto the dust grain, as well as the collisional cross section (i.e. the dust's cross sectional area),

$$\mathbf{F}_{ND} = -\pi r_d^2 m_N n_n v_{th,N} \mathbf{v}_d, \quad (2.22)$$

where  $v_{th,N}$  is the neutral thermal velocity,  $n_n$  is the neutral number density and  $\mathbf{v}_d$  is the dust grain velocity [1]. The negative sign demonstrates that the neutral drag force is a damping force.

### 2.4.4 Void Formation

The formation of a region devoid of dust grains at the onset of an external magnetic field has been observed experimentally by several authors (See fig. 1.3) [4, 5]. So far, there is little literature that quantitatively predicts and explains such a void formation. However, there is a general consensus that the magnetic field is the cause of a change in the potential profile (and hence a change in the electric field profile) of the sheath which leads to void formation.

Recently, a numerical study of the electron behaviour around a magnetic dipole by J. Gibson [7] was conducted. He proposed that within a characteristic distance from the dipole,  $\Lambda$ , the magnetic field is strong enough to dominate electron dynamics, deflecting them outwards. Electrons are unable to enter these “forbidden regions”.  $\Lambda$  is given by  $\sqrt{\frac{M\mu_0 e}{4\pi m_e v_\perp}}$ , where  $M$  is the magnetic dipole moment,  $\mu_0$  the permeability of free space and  $v_\perp$ , the component of electron velocity perpendicular to the magnetic field lines. The spatial geometry of such a forbidden region heavily depends on the electron's incoming total velocity  $v$ . The boundaries

of the forbidden region (with vertical height  $z$ ) are given by

$$z_{\pm}(r, p_0) = \sqrt{\left(\frac{q\mu_0 Mr^2}{4\pi(p_0 \pm mrv)}\right)^{\frac{2}{3}} - r^2}, \quad (2.23)$$

where  $p_0 = mbv$  for a particle with impact parameter  $b$ .  $p_0$  is called the conjugate momentum and is derived through a Lagrangian formalism [32]. It is a conserved quantity that depends on the electron's initial conditions. This means that it can be used to characterise the electron's behaviour as it interacts with the magnetic field. Different  $p_0$  values give rise to different regions that electrons can access near the magnetic dipole. More specifically, the areas accessible to particles are described by the following inequalities

$$\begin{cases} z > z_+, & p_0 \leq 0, \\ z_+ < z < z_-, & 0 < p_0 < 2\sqrt{qvm_e \frac{\mu_0 M}{4\pi}}, \\ z < z_-, & p_0 > 2\sqrt{qvm_e \frac{\mu_0 M}{4\pi}}. \end{cases} \quad (2.24)$$

Furthermore, there is a region that is inaccessible to all electrons, irrespective of their  $p_0$  value, enclosed by

$$z_0(r) = z_+ \left( r, p_0 = 2\sqrt{q \frac{\mu_0 M}{4\pi} vm_e} \right). \quad (2.25)$$

Notice that interesting things occur when the value of  $p_0$  is on the order of  $2\sqrt{q \frac{\mu_0 M}{4\pi} vm_e}$ . Using our plasma parameters, and normalising our  $p_0$  using this term, we can visualise the spatial profile of the forbidden regions with different initial electron  $p_0$  values. These are shown in fig. 2.2.

Studying the regions where electrons couple strongly to magnetic field lines provide a simplistic model of the electron distribution, which will have significant consequences in the sheath. This is because the regions devoid of electrons result in a separation of space charge, and hence a modification of the sheath's radial and vertical electric fields.

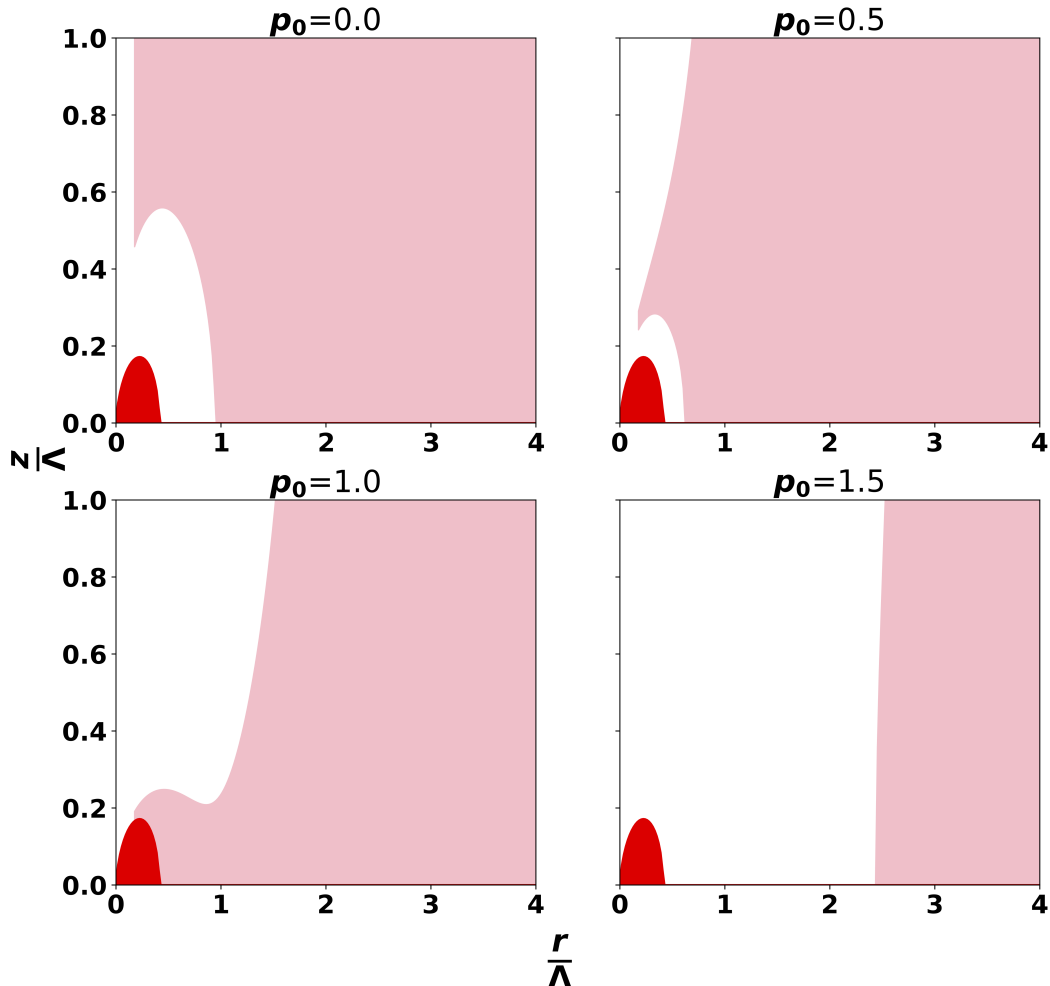


Figure 2.2: Four plots showing the regions accessible to electrons (shaded pink regions) based on their  $p_0$  value. The  $p_0$  values are normalised by  $2\sqrt{q\frac{\mu_0 M}{4\pi} v m_e}$  so that all of the interesting physics occur when  $p_0$  is near unity. Electrons are forbidden to enter the white areas. The red semicircular section near the origin is inaccessible to electrons of any initial conditions, which is a consequence of conservation laws.

On the other hand, however, this theory provides a challenge for numerical simulations, namely that the forbidden regions are not constant in their spatial profile. The value of  $p_0$  will vary wildly depending on the electron velocity and impact parameter. We get around this issue by finding an “average” forbidden region for the numerical simulation. This is done by using the absolute inaccessibility region  $z_0(r)$  (red regions in fig. 2.2) as the average forbidden

region. The most probable value of the Maxwell-Boltzmann velocity distribution (the thermal velocity) is taken as the electron velocity  $v$ . The numerical implementation of this modification is explained in Section 3.3.3.

### 2.4.5 Summary

This chapter began by studying the physics inside the sheath, where the dust grains will settle. Here, dust grains interact with the electric field generated by the negative wall potential, and with each other. The chapter then transitioned to the physics surrounding the introduction of an external magnetic field. We have provided a theory for a correction term to the ion drift velocity and studied the ion and neutral drag forces on the dust grains. We have also used a recently proposed model to study the change in electron distribution in the plasma (i.e. via forbidden regions), which alters the internal electric field that can potentially lead to void formations. These are important insights that provide the basis for later numerical simulations.

# Chapter 3

## Numerical Method

Our simulated dust grains are spherical particles with a radius of  $4.5 \mu\text{m}$  and a density similar to Melamine-formaldehyde [33]. A cylinder of diameter 40 mm is used to confine an argon plasma. The wall potential is calculated using eq. (2.4), while the charge and potential profile of the dust grain is determined using the OML theory discussed in Section 2.3.1.

Konopka used a bar magnet placed below the cylinder and claimed that the magnetic field lines are approximately vertical. Realistically, however, not only will there be deviations from a purely vertical field, but more interesting physics may arise with a non-uniform magnetic field source. Hence in our setup, a magnetic dipole is implemented at the bottom of the cylinder (similar to Saitou's experiment) with a variable z-position. Konopka had also explored the variations of pressure on the system but this will not be investigated, because we will then have to delve into dusty plasma crystal phase transitions [34].

### 3.1 Plasma Sheath and Crystal Formation

Spherical dust grains are spawned and released at randomised coordinates in the XY-plane above the cylinder and dropped into the bulk plasma. The sheath is taken to be  $10\lambda_D$  thick. A more accurate value can be obtained, but since all dust grains will settle onto the same

plane, the exact position is not crucial. The simulated dynamics of an individual dust grain is described below.

- Before the dust grain reaches the sheath, it is subject to gravity,  $\mathbf{F}_g = -mg\hat{\mathbf{z}}$ , neutral drag (eq. (2.22)) and a fluid drag force (from the collective plasma),  $\mathbf{F}_{\text{drag}} = -\frac{1}{2}\rho n C_D v^2 \hat{\mathbf{v}}$  [35]. The drag coefficient is  $C_D$ , whose value depends on the Reynolds number of the system. This was calculated in Saitou's experiment to be  $\sim 0.1$ , corresponding to a  $C_D$  of  $\sim 300$  for a spherical grain [36], as it moves through the plasma with density  $\rho$ .
- When the dust grain reaches the sheath (i.e. its vertical position  $0 < z < 10\lambda_D$ ), it experiences the electric field due to the wall potential. A parabolic potential is implemented for the walls, whereby the top edge of the sheath sits at 0 V and decreases to the floating wall potential (eq. (2.4)) at the cylinder bottom. Since the electric field  $E = -\frac{dV}{dz}$ , the vertical electric field caused by the parabolic potential is linear in space and acts to oppose the gravitational pull on the dust grain. The same potential is also radially implemented, which acts to confine the dust grains by pushing them towards the centre.
- A fully interacting picture requires that every dust grain is subject to the repulsive force from all other dust grains in the cylinder. However, as the number of dust grains  $N$  increases, the number of interactions scale  $\sim N^2$  and this quickly becomes difficult to simulate in a reasonable amount of time. Thus, to reduce the computational power required, only dust grains separated by  $10\lambda_D$  or less are considered, since by this distance the force would have decreased by  $e^{-10}$ .

Several implementations were made to ensure that the simulation is physically sound. For example, at every time step, if the unit vector from grain A to grain B is negated (flipped by 180 degrees) compared to the previous time step, it means that the grains have passed each other because they are travelling too quickly for their inter-grain potential to respond. At every time step, the net force on the dust grain is calculated, and Euler's method is used to update

the dust grain in time, whereby the updated velocity and position are given by  $v_{t+1} = v_t + a_t dt$  and  $s_{t+1} = s_t + v_t dt + \frac{1}{2}a_t dt^2$  respectively [37]. This is chosen over a more accurate method because it is less computationally expensive and any inaccuracies are not important when considering the macroscopic behaviour of the system. Each dust grain will eventually stabilise inside the sheath where the combination of all the forces under consideration cancel. The vertical component of this equilibrium position is analytically determined by equating gravity with the sheath's vertical electric field. This is checked against the simulated positions to ensure good fidelity. Furthermore, reducing the time step ensures that the numerical method does not diverge, but is done at the cost of increasing simulation time.

## 3.2 Magnetic Dipole

The introduction of the magnetic dipole results in more forces on the dust grains that must be considered at each time step. The spatial profile of the magnetic dipole is given by

$$\mathbf{B}(\mathbf{r}) = \frac{\mu_0}{4\pi} \frac{3\hat{\mathbf{r}}(\hat{\mathbf{r}} \cdot \mathbf{m}) - \mathbf{m}}{r^3}, \quad (3.1)$$

where  $\mathbf{m}$  is the magnetic moment of the dipole [38]. To calculate  $\mathbf{m}$ , the magnetic field strength at a distance  $\mathbf{r}$  is guesstimated, and eq. (3.1) is solved to find  $\mathbf{m}$ . In our case, we chose a value of  $B = 0.014T$  at  $\mathbf{r} = [0, 0, D]$  (cartesian coordinates), where  $D$  is the distance between the dipole and the equilibrium crystal position. This is to stay consistent with the experiments by Konopka and Saitou.

The dust grain's position  $\mathbf{r}$  is used to calculate the magnitude and direction of the B-field at that location. This is important in determining the three types of ion-drift velocities caused by the magnetic field (and electric field), as discussed in Section 2.4. The resultant forces on the dust grain are the Lorentz force and the ion-drag force, where the former is negligible compared to the latter. At each time step, these forces contribute to the net acceleration of each dust grain.

### 3.3 Drag forces & Dust Rotation

We can find the ion and neutral drag forces from eq. (2.13) and eq. (2.22). The latter is easily implemented as it only requires basic plasma parameters. The ion-drag, however, requires the (non-trivial) ion-drift velocity. Recall that we cannot use the standard form of the ion drift velocity (eq. (2.11)) because we must take into account the ion-neutral collisions.

#### 3.3.1 Ion-Neutral Collision Correction Factor

We proposed in eq. (2.21) that the ion drift velocity for our setup is

$$v_{\text{drift}} = \frac{q^2 \tau^2 (E_r B_z - E_z B_r)}{m^2 (1 + \omega^2 \tau^2)},$$

which accounts for the ion-neutral collisions. Here, both the electric and magnetic fields consist of radial and vertical components. To numerically test this theory, we begin by simplifying the geometry of the setup by having magnetic and electric fields that are uniform and perpendicular to each other. Let the magnetic field  $\mathbf{B} = [0, 0, B_z]$  and the electric field  $\mathbf{E} = [0, E_y, 0]$ , and ion velocity  $\mathbf{v} = [v_x, v_y, v_z]$ . Initially, let  $\mathbf{v}(t = 0) = [0, v_T, 0]$  (Note that all vectors here are described using cartesian coordinates). We can perform the same derivation shown in Section 2.4.2 to find that the average drift velocity in this scenario is

$$\begin{aligned} \bar{v}_{\text{drift}} &= \frac{\bar{\lambda}_{\text{drift}}}{\tau} = \int_0^\infty \frac{1}{\tau^2} \lambda_T(T) e^{-\frac{T}{\tau}} dT \\ &= \int_0^\infty \frac{1}{\tau^2} \frac{E_y}{B_z} \left( T - \frac{\sin(\omega T)}{\omega} \right) e^{-\frac{T}{\tau}} dT \\ &= \frac{E_y}{B_z} \frac{\omega^2 \tau^2}{1 + \omega^2 \tau^2}. \end{aligned} \tag{3.2}$$

Equation (3.2) is simply the original ion drift velocity ( $\mathbf{v}_{E \times B} = \frac{\mathbf{E} \times \mathbf{B}}{|\mathbf{B}|^2} = \frac{E_y}{B_z}$  (eq. (2.11))) multiplied by the factor  $\frac{\omega^2 \tau^2}{1 + \omega^2 \tau^2}$ , which we call the “reduction factor”. To test this, we perform two simulations:

1. In the absence of collisions, the motion of argon ions are dictated by the Lorentz equations. The cross product between the electric and magnetic field shows that the dust grains perform gyrotralional orbits in the YZ-plane and drift along the X-axis. Fourth order Runge-Kutta (RK4) method is used to update the ions in time [37].
2. In the presence of collisions, the probability at every time step,  $dt$ , for a collision with a neutral is  $1 - e^{-\frac{dt}{\tau}}$ . If a random number drawn from a uniform distribution is greater than this probability, a collision occurs (and vice versa). The dominant type of collisions between fast-moving ions and slow-moving neutrals is charge-exchange [39]. The neutral atom is ionised and we assume that the collision is elastic so it will move away with the ion's incoming thermal velocity but in an isotropic, randomised direction.

The reduction factor is computed by taking the ratio between the drift distances (after 3s) with and without collisions. Each simulation with a different  $\omega \times \tau$  value is run 100 times and the error interval at 95% confidence is computed via the Bootstrap method [40]. To ensure that the RK4 method does not diverge (or decay to zero), the total ion energy without collisions must be constant throughout the simulation.

### 3.3.2 Curvature and Grad-B ion drifts

Recall that a non-uniform magnetic field causes ions to drift according to eq. (2.12). The main non-trivial component to be determined here is the gradient of the magnetic dipole,  $\vec{\nabla}B$ . This is analytically derived in cylindrical coordinates and then numerically implemented.

### 3.3.3 Internal Electric Field Modification

Recall from Section 2.4.4 that we determined an average region near the magnetic dipole where electrons are forbidden to enter. This region is denser in positive charges compared to the rest of the sheath, and the boundary is determined through eq. (2.25). The volume of revolution

around the z-axis of this region is computed through numerical integration. We can figure out the amount of charge that is displaced from this region,  $Q_{\text{displaced}}$ , by integrating the electron number density (Maxwell-Boltzmann distribution) over the forbidden region. To simulate the charge separation, a lattice of evenly spaced, positively charged ions (with net charge  $Q_{\text{displaced}}$ ) is introduced inside the forbidden zone. They represent the fact that this region no longer contains a collectively neutral plasma. The number of displaced electrons is added into the rest of the cylinder but has a negligible effect on the background electron number density because the forbidden zone volume is much smaller than the sheath volume.

In light of the new distribution of charge, the electric field at any point in the cylinder must now include the sum of the electric fields due to the lattice of ions. However, the number of calculations needed to find the total force on the dust grains due to the ion lattice will scale  $\sim N_{\text{ion}} \times N_{\text{dust}}$ , where  $N_{\text{ions}}$  is the number of ions in the lattice and  $N_{\text{dust}}$  is the number of dust grains currently in existence. This is computationally expensive. Thus, the electric field experienced by dust particles inside the forbidden region is computed through bilinear interpolation with the nearest lattice ions [41]. Dust grains outside the forbidden region will feel a screened potential (recall from eq. (2.9) that the screened potential is exponentially decaying) from the forbidden region, by assuming that it is a point source at the centre, while grains near and inside boundaries will experience the interpolated field. The profile of the interpolated electric field at different points in the RZ-plane is shown in fig. 3.1.

### 3.3.4 Summary

This chapter numerically implements the theory discussed in Chapter 2. Firstly, forces on dust grains in the absence of a magnetic field are considered. This should lead to crystal formation with the anticipated hexagonal packing seen in fig. 1.1. After the magnetic dipole is inserted, the dust grains are now further subject to the Lorentz force, ion drag, and the force due to the

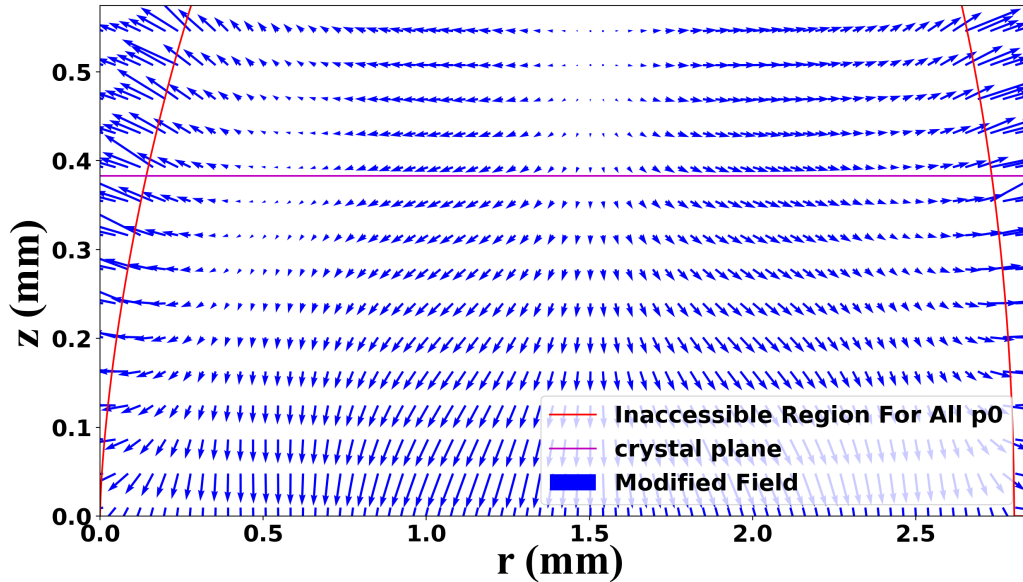


Figure 3.1: Visualisation of the electric field inside the forbidden region due to a lattice of positive ions. The blue arrows show the (normalised) interpolated electric field at their specific spatial coordinate, due to the lattice of ions. Since dust grains are negatively charged, the force exerted on them by the electric field is in the opposite direction to the arrows. The magenta line denotes the crystal plane.

modified electric field. At each time step, the net acceleration on the dust grain is calculated and the dust grain is updated in time through Euler's method.



# Chapter 4

## Results

There are several variables that one can change in the simulation, such as magnetic field strength, magnetic field position, dust grain sizes, etc. The most influential object is no doubt the magnetic dipole. Moving it up and down the Z-axis allows us to achieve different field geometries, i.e. non-uniform when the dipole is placed near the cylinder, and (approximately) vertical when it is far away.

### 4.1 Crystal Structure

Figure 4.1 shows the equilibrium positions of 1000 dust grains in the XY-plane. As they are monodisperse and equal in mass, they form a single layer with equal vertical coordinates. Notice that the equilibrium separation distances increase towards the crystal edge, and the crystal looks less structured. This edge effect arises because grains near the edge are not as evenly surrounded (thus do not experience as many inter-grain forces) compared to those near the centre. Furthermore, though the majority of the crystal display hexagonal packing, there are sites with fewer, and sites with more than six neighbours. More detailed analyses of the structure will not be done and instead, we direct our attention to the project's principal concern — magnetic field effects.

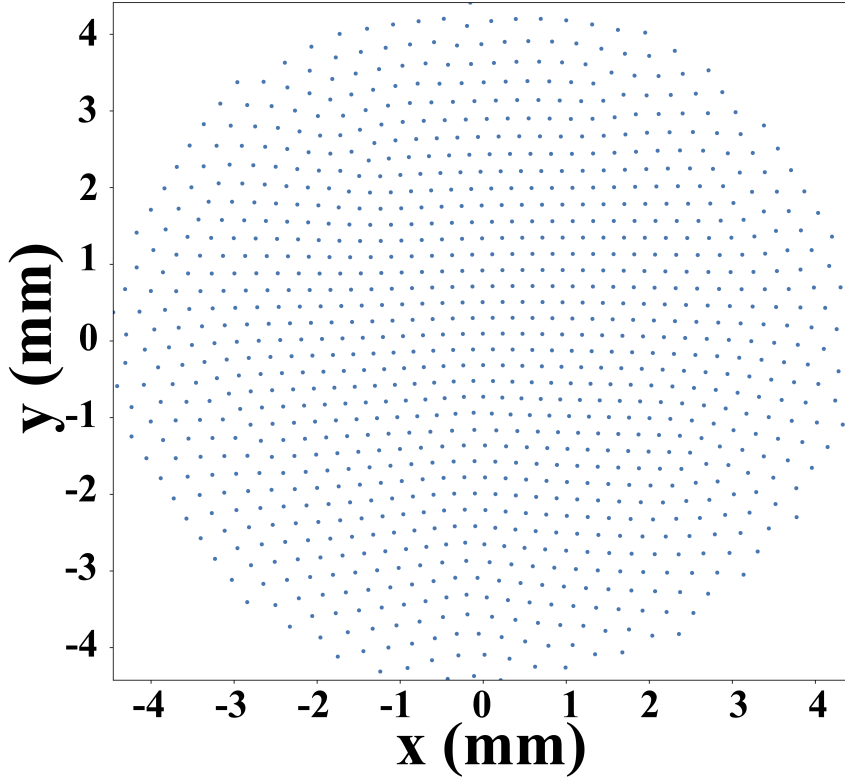


Figure 4.1: The coordinates of 1000 dust grains settled into their equilibrium positions inside the sheath. Overall, the structure shows a hexagonal lattice. However, there are sites with fewer and sites with more than six neighbours.

## 4.2 Magnetic Field Effects

### 4.2.1 Ion-Neutral Collision

Recall that in order to obtain a more physical value for the  $\mathbf{E} \times \mathbf{B}$  drift velocity, we proposed a correction to the drift velocity in Section 3.3.1 that takes into account the ion-neutral collisions.

Figure 4.2 shows the result of the simulation that tested the validity of our theory for this correction term. Several values of  $\omega \times \tau$  were examined. This signifies testing different magnitudes of magnetic field strengths, because  $\omega = \frac{qB}{m_i}$ . As there is no fitting done, we conclude that the fit is good as the bootstrapped errors at 95% confidence effectively intersect

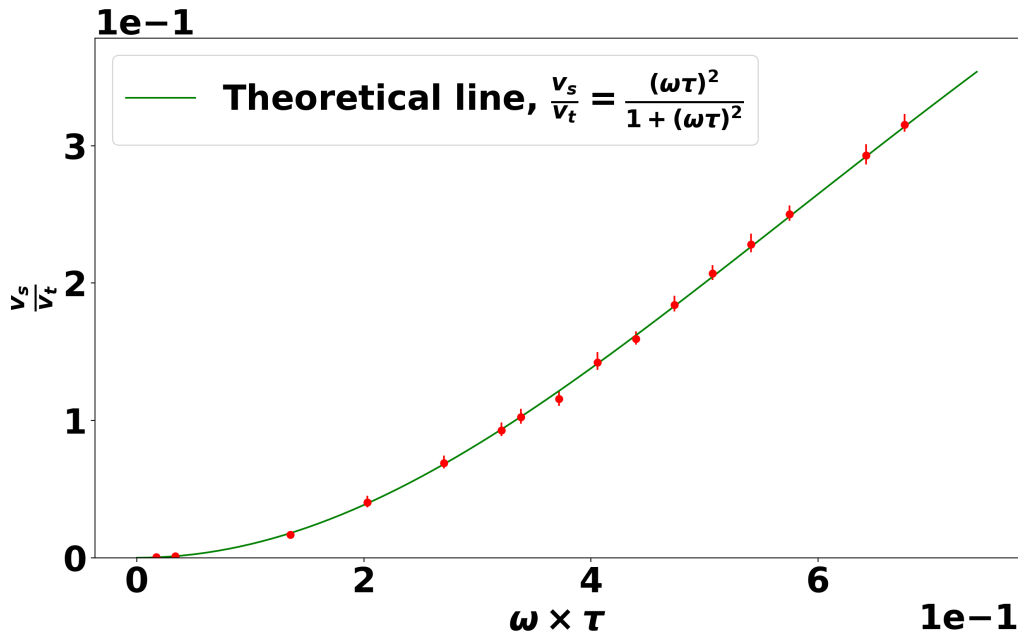


Figure 4.2: The plot of the ratio between ion drift velocities against  $\omega \times \tau$ .  $v_s$  is the simulated drift velocity including ion-neutral collisions, while  $v_t$  is the theoretical drift velocity without considering collisions. Their ratio represents the fractional reduction in the ion drift velocity due to collisions with neutrals. Each  $\omega \times \tau$  simulation is run 100 times and errors at 95% confidence are calculated using the bootstrap method.

with the theoretical line. This figure implies that for regions with small magnetic fields, the numerator of the theoretical curve equation,  $(\omega\tau)^2$  dominates and causes the drift velocity to approach zero. This is physically intuitive, as the magnetic field is not strong enough to deflect the ions and their motion is dominated by randomised, isotropic collisions. On the other hand, the ratio approaches one in the limit of large magnetic fields. This is because the stronger magnetic field can easily recover the original drift of the ion even when it is knocked off course.

### 4.2.2 Void formation

Now, let's enquire into the crystal's rotational behaviour. Figure 4.3 shows the state of a crystal of size  $N=250$  in the absence (a) and presence (b) of a magnetic dipole. The only difference in the simulation is that the modified electric field profile shown in fig. 3.1 is included in addition

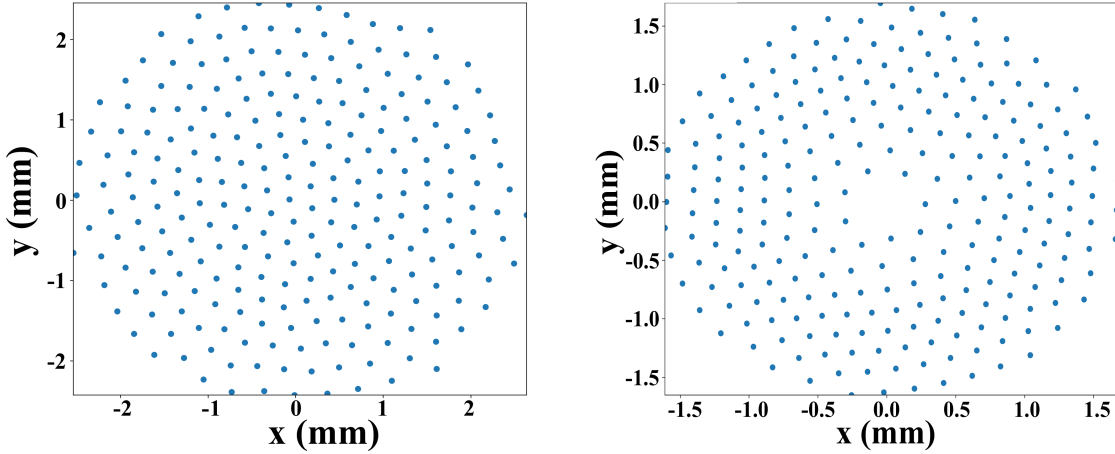


Figure 4.3: (a) The shape of the crystal (with  $N=250$  dust grains) rotating in the presence of a magnetic dipole placed. The electric field inside the sheath is not modified using Gibson's methods. (b) shows the same crystal setup but also includes the modification of the internal electric field. The void formed here has a diameter of order  $\sim 1$  mm.

to the sheath's electric field. As the crystal is rotating, the absence of the void in fig. 4.3(a) proves that the void in fig. 4.3 (b) could not have been formed from centrifugal effects.

Notice further that the crystal has shrunk in size upon the inclusion of the modified electric field. This is intuitive as the grains outside of the forbidden region are attracted towards the positive lattice of charge in the centre.

### 4.2.3 Crystal Rotation

We now investigate in more detail the macroscopic rotational behaviour of the dusty plasma crystal. This is non-trivial to study because not only are there many forces acting on the dust grains at any instance in time, but their magnitude and direction also vary depending on the spatial profile of the magnetic dipole.

First, the dipole is placed 5cm away so that the field lines are essentially vertical in the vicinity of the crystal. The magnitude and direction of dust grain rotation is shown in fig. 4.4. The crystal exhibits rigid rotation. In this scenario, the dust grain speed increases linearly with radial distance and the whole crystal appears to rotate as a rigid body. The magnetic field in

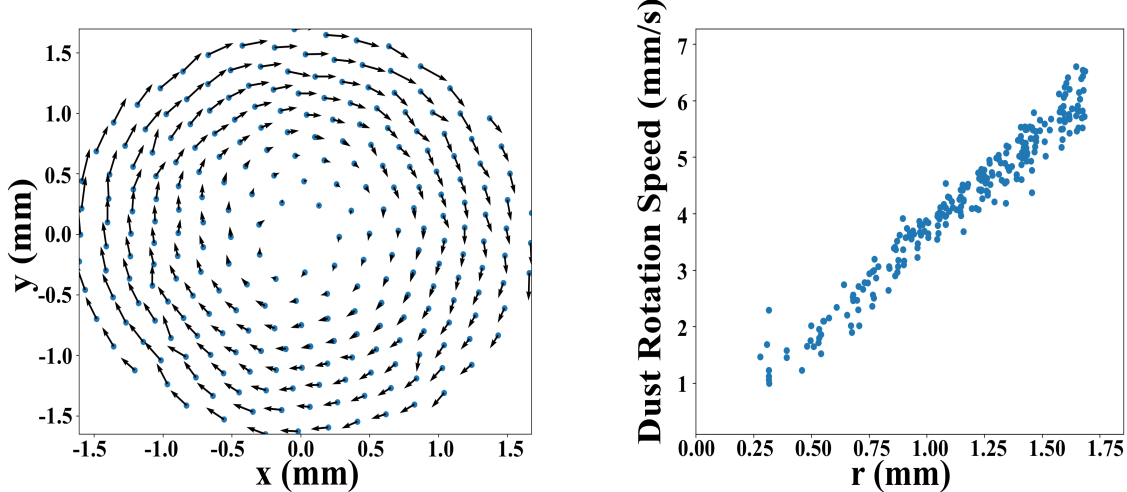


Figure 4.4: (a) Plot of the crystal rotation direction for each dust grain after 1s ( $N=250$  dust grains). The dipole is 5cm below the cylinder and the arrows are normalised to visualise the general rotational behaviour. (b) Plot of the individual dust grain speeds as a function of their radial distance from the cylinder center.

this case is approximately vertical across the dust crystal. This means that the ion drift velocity  $\mathbf{v}_{E \times B}$  has a consistent magnetic component,  $\mathbf{B}$ , and a linearly increasing electric component  $\mathbf{E}$  towards the edge of the crystal. This intuitively results in a linearly increasing ion drag force as one moves away from the centre, and hence rigid rotation is demonstrated.

We now move the dipole closer towards the cylinder, with a separation distance of 5mm from the bottom to resemble the thickness of the lower electrode. In this scenario, the magnetic field is no longer approximately uniform inside the cylinder. Instead, it is strongest in the central axis and the curvature of the field towards the sides (and direction change) occurs within the crystal.

The dust grain speed profile is shown in fig. 4.5. This no longer exhibits rigid rotation but instead, it shows differential rotation. Here, the ions near the centre are strongly affected by the magnetic field. The  $\mathbf{E} \times \mathbf{B}$ , curvature and grad-B drift velocities are all large (compared to their respective values at larger radial positions) and contribute to a large ion drag force. As one moves outwards, the drift velocities are suppressed by the rapidly decreasing vertical components of the magnetic field lines, causing the ion drag force to decrease. Additionally,

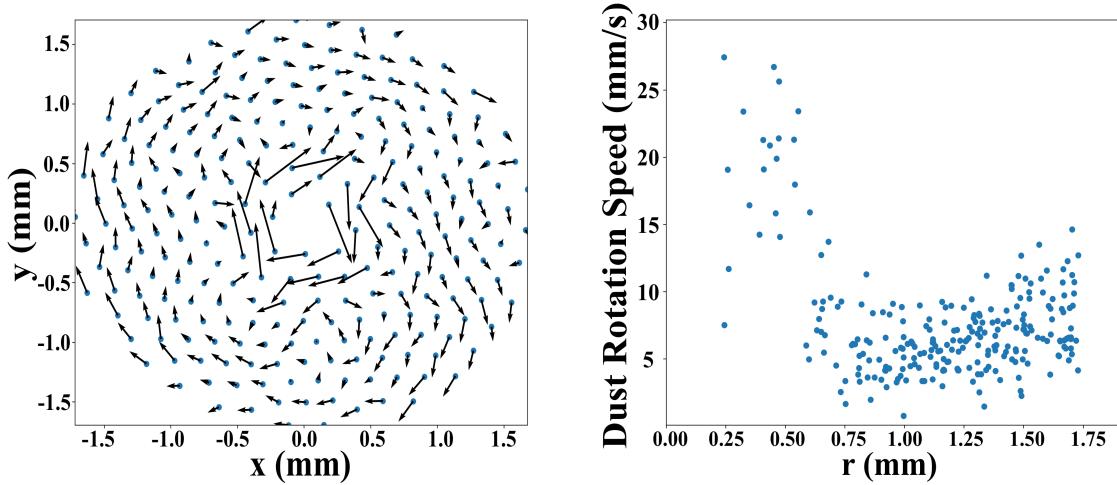


Figure 4.5: (a) Plot of the crystal rotation direction for each dust grain after 1s ( $N=250$  dust grains). The dipole is 5mm below the cylinder and the arrows are normalised to visualise the general rotational behaviour. (b) Plot of the individual speeds of the dust grain as a function of their radial distance from the cylinder centre.

the directions of the magnetic field lines are also changing. The net result is that the rotational behaviour of the dust grains is no longer smooth like that in fig. 4.4. Instead, it follows a zig-zag pattern, which is reminiscent of the experimental observations discussed in Section 1.2.2. This pattern does not have any characteristic frequencies. This zig-zag motion is likely the result of collisions with surrounding particles and is thus considered to be random in nature.

We have thus shown that there exist at least two regimes for the dust grains' rotational behaviour — rigid and differential — depending on the geometry of the external magnetic field.

In the simulation of the differential rotation, one would expect the dust to start rotating in the opposite direction when the magnetic field changes direction (assuming the electric field does not change in direction). In the case of fig. 4.5, the magnetic field starts to becomes parallel at  $r \sim 1$  mm, and from there points outwards and downwards. However, this is not clearly visible in fig. 4.5. To explain this, let us investigate the ion drift velocity. Near the centre of the crystal, the component of  $E_r$  points outwards and the component of  $B_z$  points upwards. This results in a clockwise rotation as seen in figs. 4.4 and 4.5. As one moves outwards, the magnetic field becomes parallel to the crystal layer, before starting to point downwards. At

the stage when it is parallel to the crystal, the cross product between the  $E_z$  component of the electric field and the  $B_r$  component still points in a clockwise direction. At the point where the downward magnetic field component dominates over the parallel component, the direction of ion drift should now be counter-clockwise. However, at this stage, the magnetic field strength is very small compared to that at the centre. This means that the ion drift velocity is very much subdued (due to collisions with neutral atoms), and the resulting ion-drag force is not enough to overcome inter-grain interactions. Therefore, it is more likely that the rotating dust grains in the inner circles will push the outer dust grains along. Thus, collectively there is no visible, aggregate rotation in the opposite direction.

To show the importance of ion-neutral collisions and the reduction factor proposed in Section 2.4.2, let us consider the case when they are neglected (i.e. using the equation  $\mathbf{v}_{\text{drift}} = \frac{\mathbf{E} \times \mathbf{B}}{|\mathbf{B}|^2}$  for ion drift). Now, not only will dust grains rotate in different directions when the magnetic field changes directions, but their speeds will also become so large that the centrifugal force of the rotation is enough to create a void. This is not feasible because experimentally, the motion of the dust grains are on the order of  $\sim 1$  mm/s, and it is widely agreed that the centrifugal force is not enough to cause void formation. Figure 4.6 shows the unphysical nature of the simulation when neglecting the ion-neutral collisions.

To obtain the results in fig. 4.6, the ion-drift velocity had to be reduced by a factor of  $10^4$  in order to make sense of the resulting velocities, because otherwise, the rotational speed will rapidly reach up to several meters per second even within the short simulation time of 0.1 s. Furthermore, as time passes, the dust grains in fig. 4.6 will spiral out further as the centrifugal force dominates. This re-enforces the necessity of ion-neutral collisions, which makes the simulation more credible.

So far we have looked into the void formation and the effect of magnetic field's *geometric* profile on the rotational behaviour of the dust grains. It will be interesting to study the effect of magnetic field strength on the speed of dust grains at a specific radial distance. For this,

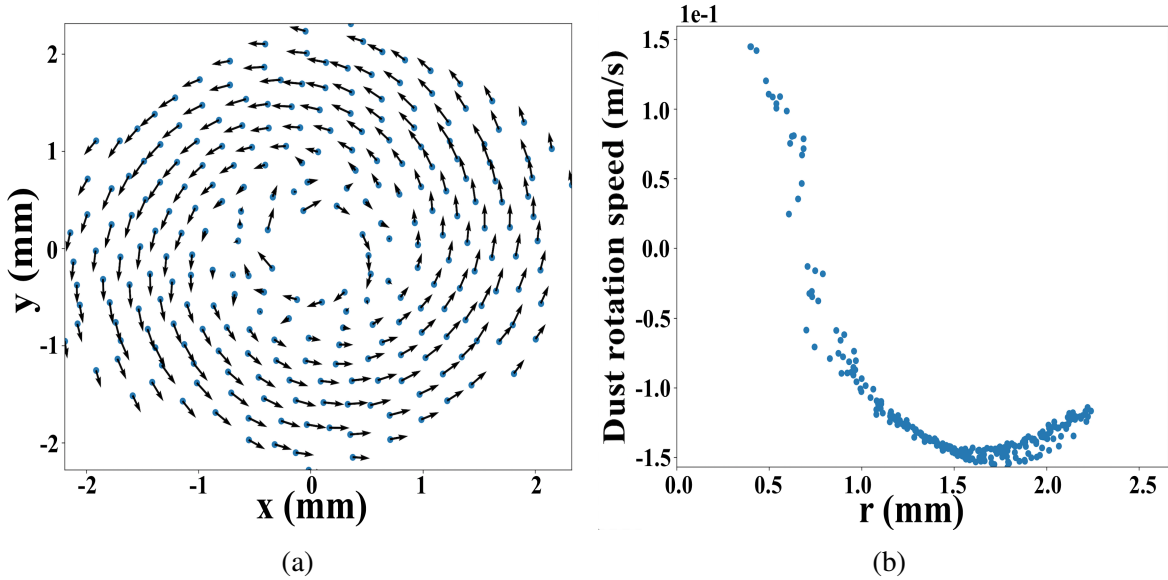


Figure 4.6: (a) Plot of the crystal rotation direction for each dust grain after 0.1s ( $N=250$  dust grains). Notice that the dust velocities already reach several cm/s in this short time. The dipole is 5 mm below the cylinder and the arrows are normalised to visualise the general rotational behaviour. There is no inclusion of the modified electric field and yet there is void formation. (b) Plot of the individual velocities of the dust grain as a function of their radial distance from the cylinder centre. Negative velocities are used to denote counter-clockwise rotations.

we will “turn off” the modified electric field. This is because otherwise, we would have to recalculate the forbidden region every time we change the magnetic field strength (this will lead to a different void and crystal size). This may complicate the underlying relationship between the dust rotation speed and magnetic field strength. In previous analyses, the magnetic dipole strength was taken to be 0.014T at the crystal layer. This value is now altered and the results are shown in fig. 4.7.

The dust grain speed appears to plateau at large magnetic field strengths. This may be due to the fact that as the dust speed increases with a larger ion drag, the neutral drag force increases correspondingly in the opposite direction. The increase in dust speed from  $\sim 2$  mm/s (at field strength of  $\sim 0.014$  T) to  $\sim 60$  mm/s per second means that the centripetal force  $F_{\text{centrifugal}} = \frac{m_d v_d^2}{r}$  is increased by a factor of  $\sim 900$ . The centripetal force now dominates as it exceeds the ion-drag force (which is of order  $\sim 10^{-14}$ ) by  $\sim 10$ . The magnetic field strength

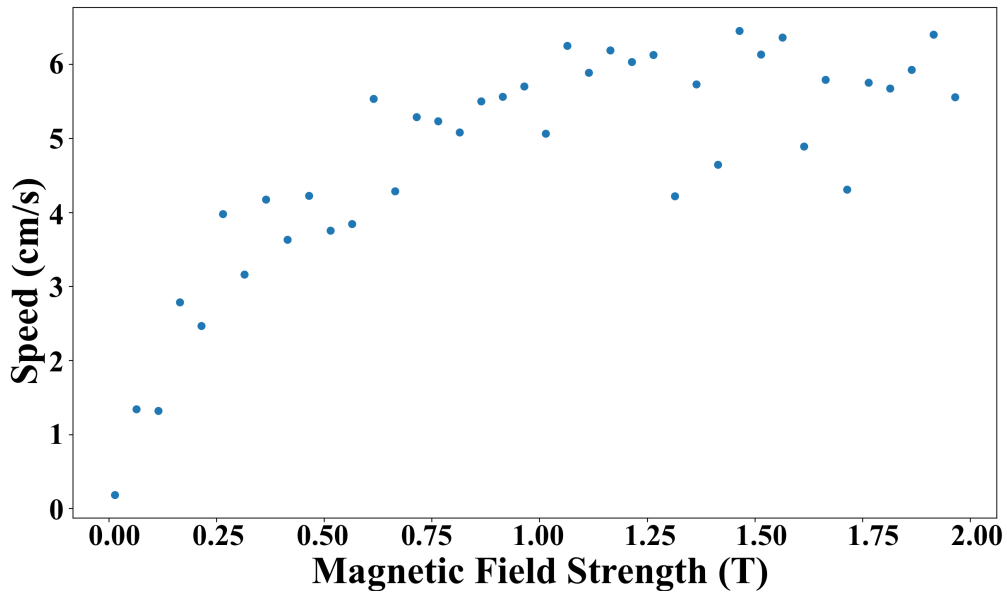


Figure 4.7: Plot of the magnetic strength at the crystal layer against the rotational speed of a dust grain at a distance of 1 mm from the cylinder centre. The dipole is 1cm below the cylinder. This plot shows that there is a plateauing behaviour of the dust speed at large magnetic field strengths.

used in this range is much larger than that used in literature experiments, and effects due to the centrifugal force at such large dust speeds were not investigated by the relevant literature experiments.



# **Chapter 5**

## **Discussion**

### **5.1 Comparisons with literature**

We have now gathered simulated data governing the dynamics of dusty plasma crystals in an external magnetic field, and would like to compare these findings with real experiments. The exact plasma and setup parameters provided by literature vary slightly, but are within the same order of magnitude. The specifications used in the simulations involving magnetic fields were motivated by those used in the experimental works of Saitou and Konopka. Some parameters, such as the radial profile of the cylinder walls and the dust grain charge, were not precisely given and had to be guesstimated. Furthermore, a magnetic dipole was used instead of a finite bar magnet (used in experiments) to simulate the magnetic field. Overall, we expect the general behaviour of the plasma crystal to be predominantly similar to what is observed. We would also like to compare the order of magnitude of our simulated results to the experimental observations.

### 5.1.1 Plasma Crystal Structure

Before delving into experiments involving magnetic fields, we begin by comparing our dust crystal structure with a numerical simulation of a crystal lattice done by L.S. Matthews et al [42]. They have also employed a cylinder wall potential that was parabolic in nature.

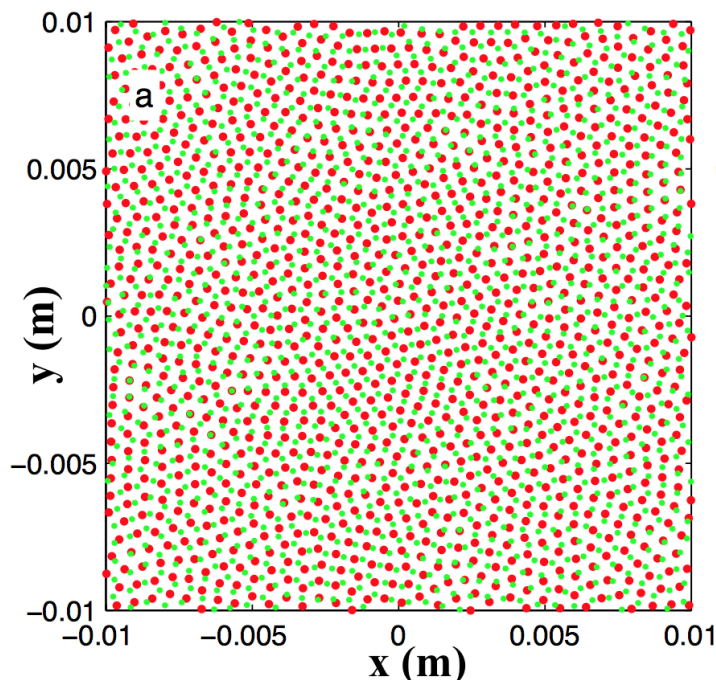


Figure 5.1: Matthews et al simulation of dusty plasma crystal with two different sizes of dust grains [42]. The plot shows the equilibrium coordinates of particles with  $6.5 \mu\text{m}$  (green) and  $9 \mu\text{m}$  (red) diameters.

The average inter-particle spacing for their simulation was  $6\lambda_D$ , while for our crystal it is  $5\lambda_D$ . The difference comes from a range of assumptions that differ between the two simulations. For example, Matthews et al guesstimated the values of the dust charge and surface potential (while we calculated them using OML theory), and their calculations yielded a larger Debye length compared to our setup. This means that the inter-grain repulsion in their model decays slower than that in our model, resulting in a larger average equilibrium grain-separation distance.

### 5.1.2 Saitou's experiment

Saitou created an argon plasma using radio-frequency discharge and placed a small magnet underneath the crystal. This is very similar to our setup. Recall that we have predicted a forbidden region for electrons under the assumption that the magnetic field is caused by a point dipole, which led to a simulated void formation. The fact that Saitou's small magnet can be approximated as a dipole is the reason why we can justify comparing our void formation to his observations.

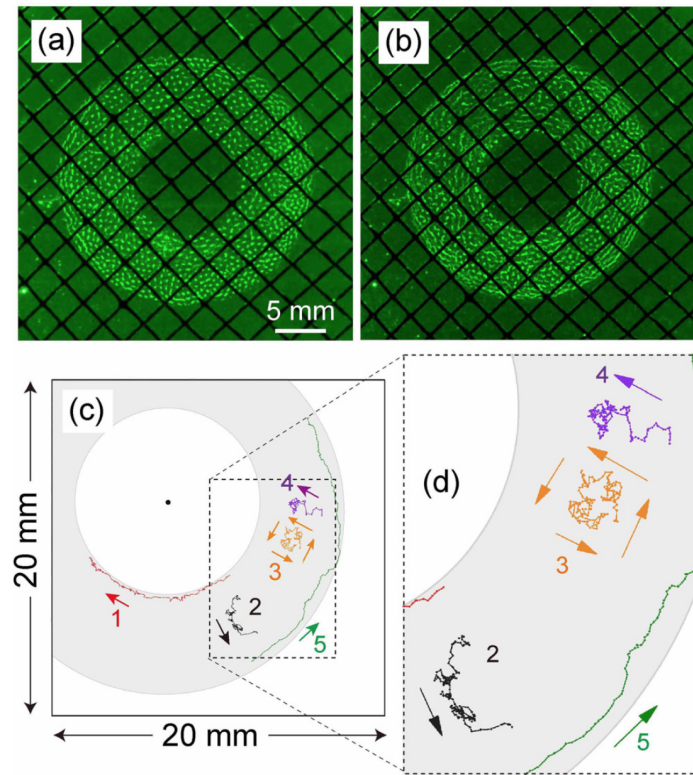


Figure 5.2: Experimental results by Saitou [5]. (a) Plot of the dust grains' spatial distribution at a specific instance of time. (b) The average orbit performed by dust particles in  $\sim 30$  s. (c) and (d) Qualitative drawings of different dust grain trajectories.

Figure 5.2 shows the results of Saitou's experiment. There are several things to note:

- The void formed had a radius of  $\sim 5$  mm, while our simulation resulted in a void of  $\sim 0.5$  mm (See figs. 4.3 to 4.5). This is expected as our theory generalised a simple

electron kinetics model and also took an average over all possible geometries of the electron inaccessibility region. The method of setting up the deflection of electrons from this region was to introduce a lattice of positive ions, rather than a more accurate solution that could be obtained via solving Poisson's equation. Our simulation is not a full molecular dynamics simulation that included the plasma ions, but instead considered the net macroscopic effects on the dust grains from complex plasma interactions. Furthermore, the potential profile inside the sheath was not explicitly stated in literature experiments and could have easily been different compared to our parabolic assumption. However, the general feature of the void, i.e. a well defined circular region at the crystal centre, was acquired.

- The dust rotation speeds were experimentally reported to be  $\sim 0.5$  mm/s, while our dust speeds were of  $\sim 1 - 10$  mm/s. This is heavily sensitive to the placement of the magnetic dipole and the value of the magnetic dipole moment, which were guesstimated. Moreover, disagreements between simulated and real potential profile (argued previously) also contribute to this disparity.
- Dust grains near the crystal centre travelled in a clockwise direction (the direction of travel seen in our simulations), while grains on the outer edge moved in the opposite direction. The reason for this was that the particles used in Saitou's experiment were of different sizes and masses (i.e. not mono-disperse nor of equal densities), so that they stabilised at different layers inside the sheath. Since their void size was much larger, the dust grains at the outer edge settled into regions where the magnetic field was flipped in direction. This caused the ion drag force to change direction and hence the particles rotated in a counter-clockwise manner. In our simulation, we did not observe this counter-clockwise rotation even when the magnetic field changed direction, and we attributed this to the fact that the magnetic field is from a point dipole, and becomes too weak at larger distances, where the ion drag is seriously suppressed. This problem can be investigated

in future simulations by invoking a finite magnetic source, with farther reaching and more realistic magnetic field lines. Furthermore, experimental observations were over the course of  $\sim 30$  s and the speeds were fractions of a millimetre per second. On the other hand, our simulations lasted  $\sim 3$  s (due to long run-times), and the possibility of achieving counter-rotation after this length of time may have been overlooked.

### 5.1.3 Konopka et al's experiment

Saitou focused on the variation of dust grain speeds at different heights inside the sheath. Konopka, on the other hand, studied the radial distribution of the speeds.

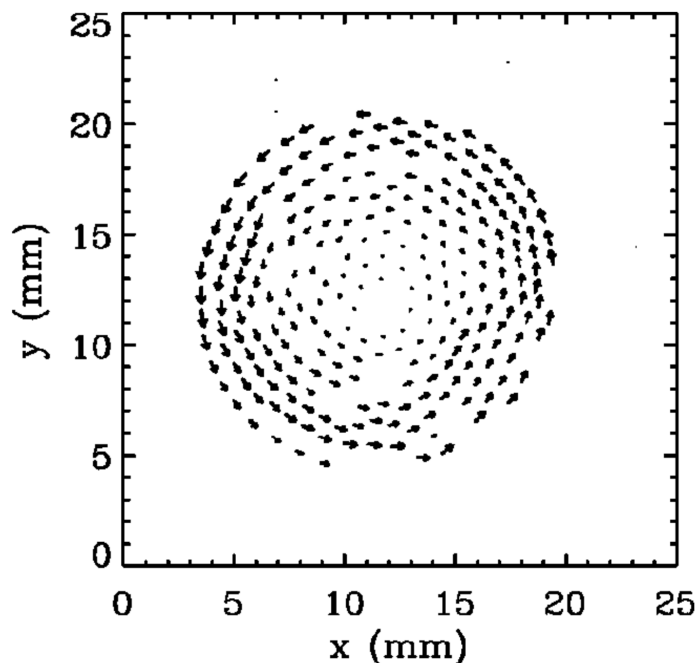


Figure 5.3: Experimental result by Konopka [4]. Plot of crystal rotation with  $N=250$  grains. This is the same number of grains used in our simulations.

There are several things to note here:

- Konopka used a bar magnet which he claimed to provide a virtually vertical magnetic field. A void was formed but we will refrain from comparing it to our theory because this magnetic field geometry would not result in the same electron distribution as that caused

by a magnetic dipole. Therefore the forbidden regions would differ, creating a different modified electric field. However, fig. 4.4 from our results attempted to approximate a vertical magnetic field by moving the dipole downwards. In this limit, we successfully reproduced rigid rotation, which was reported by Konopka in fig. 5.3.

- The speed of rotation was on the order of  $\sim 0.5$  mm/s, similar to that reported by Saitou, while our dust grains moved on the order of  $\sim 1 - 10$  mm/s. The reasons for the discrepancies are the same as those mentioned when comparing to Saitou's results.
- The size of the crystal was several times larger than our simulated crystal. This could be due to the calculations of our plasma parameters. For example, we used simple OML theory and neglected secondary effects, which meant that the dust grain charges were likely different from those in experiments. The exact profile of the potential was not known and the actual drop off behaviour may be different than the assumed parabolic profile. If our confining potential was smaller in magnitude, with a higher drop off rate, we could obtain smaller rotation speeds. Finally, the system was also very sensitive to the magnetic strength and spatial profile, which we approximated using the far-field profile of a magnetic dipole.
- The direction of crystal rotation was counter-clockwise. This was because the magnetic field used by Konopka was pointing downwards everywhere (see fig. 1.2), while our dipole field pointed upwards, so that the experimental ion drift was in the opposite direction compared to our simulations.
- Konopka also investigated the effects of pressure on the system and fig. 1.3 showed a much larger void being formed. This was not investigated in the project but could be a good route for future investigations.

## 5.2 Improvements to the model

So far, we have noted several discrepancies from the comparison of our results to real experiments, and suggested reasons behind the deviations. There are several improvements to the model that can be made to help bridge the gap between these inconsistencies. Here is a list of suggestions ranked in order of importance.

- **The implementation of the modified electric field in the sheath.** This was based on a simple theory of electron kinematics. Recall that the region inaccessible to a specific electron was heavily dependent on the electron velocity and impact parameter. One can obtain a more accurate model for the electron distribution by solving Poisson's equation, or performing a full molecular dynamics simulation of the charged particles in the plasma. However, we have instead simplified the picture greatly by averaging over the range of different forbidden regions. Moreover, the electric field caused by the change in charge distribution was modeled through setting up a discrete set of ions in a lattice, and using interpolation to calculate the resulting field at any point. Again, this can be improved by implementing a full MD simulation.
- **The accuracy of plasma parameters.** We can improve the model's validity by using more accurate models for the magnetic field profile, electric field profile, dust charge, and sheath thickness to name a few. The system is very sensitive to these parameters, and the model can be made more realistic by taking into account more phenomena that can contribute to macroscopic behaviour, such as the effect of ions streaming into the sheath [43]. The effects of temperature and pressure were also neglected in the simulations, but have been shown (by Konopka) to have significant effects on the void formed.
- **Multiple crystal layers and inter-grain forces.** Saitou showed that particles of different sizes formed multi-layered crystals. However, this project focused on the physics of a

single crystal layer. This is not only because it reduces computational time, but also because there are inter-layer interactions that introduce further complications. Finally, a more detailed theoretical study of the force between two dust grains has shown that it includes an attractive term at large distances [14], which we have neglected in our model.

This project focused on constructing a numerical framework that studies interactions between dusty plasma crystals and magnetic fields, as well as verifying the basic behaviours that have been experimentally observed. Despite the observed discrepancies, the model provides the foundation for future work into the quantitative analyses of crystal dynamics as a function of the magnetic field strength and geometry. For example, a good starting point is to investigate magnetic field effects on crystal and void sizes.

# Chapter 6

## Conclusion

The aims of the project were to first develop a simulation of the spontaneous formation of a dusty plasma crystal, by studying the forces experienced by dust grains as they enter a confined plasma. Then, it sought to investigate the effects of a magnetic dipole on the crystal and finally, determined whether the model was able to illustrate the underlying physics observed in real experiments.

We began by using common plasma parameters used in low-temperature discharge experiments to calculate potentials generated at the cylinder walls and dust grain surfaces. This was done by considering the flux of ions and electrons onto the respective surfaces at equilibrium. The flux of ions and electrons onto the cylinder walls were responsible for setting up the electric field inside the region of interest, called the sheath. OML theory was used to calculate the dust grain charge, which was important in determining its interactions with the plasma and other dust grains. The relevant forces under consideration so far were electric field forces, dust-dust repulsion, gravity, and neutral and fluid drag. We successfully demonstrated the formation of a single-layered dusty plasma crystal with a hexagonal packing structure.

The second stage was to implement the effects of a magnetic dipole located below the cylinder. Specifically, we focused on the drag forces on the dust grains and the modification of the electric field inside the sheath. The total drag force consisted of the ion, neutral and

fluid drag. The contributions to the ion drag force originated from three types of ion-drifts. The dominant type of drift was called the  $\mathbf{E} \times \mathbf{B}$  drift, which came from the cross product of the electric and magnetic fields. This drift equation was, however, flawed in the sense that it diverged at small values of magnetic fields, which was unphysical. To combat this issue, we proposed a correction factor that suppressed the divergence of this equation, by considering the physics of ion-neutral collisions. A simulation of this was performed which validated our proposed correction factor. The corrected ion-drift velocities were crucial to the simulation. This was because the resulting ion drag force allowed the crystal to rotate with a physically feasible velocity. A study of the dust grain speed distribution as a function of radial distance from the crystal centre revealed two regimes abided by the speed profile — rigid and differential rotation. The former case saw that the crystal rotated as a whole as if it were a rigid body. This occurred when the magnetic dipole was placed “far” away such that the field lines at the crystal plane were essentially vertical. Bringing the dipole closer to the cylinder meant that field lines became non-uniform, which resulted in differential rotation. Here, dust grains near the centre rotated faster than those near the crystal edge.

Another novel aspect of the project was the successful simulation of a void as a result of the magnetic field. This was motivated by the theories from Gibson’s thesis, which studied the electron kinetics in the presence of a magnetic dipole. The existence of a “forbidden” region, inaccessible to electrons, near the vicinity of the dipole was calculated. This absence of electrons was numerically simulated by introducing a lattice of positive charges in the forbidden region, which modified the sheath electric field. As a result, a void was formed, but the size was several times smaller than what was experimentally observed. This was attributed to the simplicity of the model, and the fact that the simulation was very sensitive to parameters such as the position and strength of the magnetic dipole. These issues inspired ideas for future improvements to the model that could help further reconcile simulations and experimental results (proposed in Section 5.2). For example, solving Poisson’s equations for the charge

distribution in the sheath could lead to a better prediction of the forbidden region. We could also make the model more authentic by considering effects such as secondary charging processes, multiple crystal layers and having a finite magnetic field source.

On the whole, the model achieved its goal, which was to portray the qualitative dynamics and behaviour of crystal formation and rotation. Ultimately, it can be used for further investigations into a wide variety of phenomena regarding magnetic fields and dusty plasma crystals, in addition to those explored in this project.



## **Acknowledgements**

I, the author, would like to thank Dr. Micheal Coppins for his invaluable guidance throughout the project. He was always eager to meet and discuss results, and often offered helpful insights to the results obtained. I would also like to thank the Dr. Joseph Gibson for the fruitful discussions regarding his PhD research that was a crucial stepping stone to the development of the model investigated in this project. Furthermore, I would like to express my gratitude to the PhD students under Dr. Coppins' supervision, and Professor John Allen for the interesting weekly discussions on general dusty plasmas physics. This project has really inspired me to potentially work with plasma physics research as a full time academic profession in the future. Finally, I would like to thank Tom du Val, another physics MSci student, for his help in proofreading and grammar checking the final draft.



# References

- [1] G. V. Paeva, “Sheath phenomena in dusty plasmas,” tech. rep., Citeseer, 2005.
- [2] H. Thomas, G. Morfill, V. Demmel, J. Goree, B. Feuerbacher, and D. Möhlmann, “Plasma crystal: Coulomb crystallization in a dusty plasma,” *Physical Review Letters*, vol. 73, no. 5, p. 652, 1994.
- [3] G. Morfill and H. Thomas, “Plasma crystal,” *Journal of Vacuum Science & Technology A: Vacuum, Surfaces, and Films*, vol. 14, no. 2, pp. 490–495, 1996.
- [4] U. Konopka, D. Samsonov, A. Ivlev, J. Goree, V. Steinberg, and G. Morfill, “Rigid and differential plasma crystal rotation induced by magnetic fields,” *Physical Review E*, vol. 61, no. 2, p. 1890, 2000.
- [5] Y. Saitou, “Motions of dust particles in a complex plasma with an axisymmetric nonuniform magnetic field,” *Physics of Plasmas*, vol. 23, no. 1, p. 013709, 2016.
- [6] D. Jiles, *Introduction to magnetism and magnetic materials*. CRC press, 2015.
- [7] J. Gibson, “Theoretical and computational studies of magnetized dusty plasmas,” 2018.
- [8] W. Farrell, W. Kurth, D. Gurnett, A. Persoon, and R. MacDowall, “Saturn’s rings and associated ring plasma cavity: Evidence for slow ring erosion,” *Icarus*, vol. 292, pp. 48–53, 2017.
- [9] A. Y. Pigarov, S. Krasheninnikov, T. Soboleva, and T. Rognlien, “Dust-particle transport in tokamak edge plasmas,” *Physics of plasmas*, vol. 12, no. 12, p. 122508, 2005.
- [10] V. E. Fortov and G. E. Morfill, *Complex and dusty plasmas: from laboratory to space*. CRC Press, 2009.
- [11] V. Fortov, A. Ivlev, S. Khrapak, A. Khrapak, and G. Morfill, “Complex (dusty) plasmas: Current status, open issues, perspectives,” *Physics reports*, vol. 421, no. 1-2, pp. 1–103, 2005.
- [12] V. E. Fortov, A. G. Khrapak, S. A. Khrapak, V. I. Molotkov, and O. F. Petrov, “Dusty plasmas,” *Physics-Uspekhi*, vol. 47, no. 5, pp. 447–492, 2004.
- [13] C.-L. Wang, G. Joyce, and D. R. Nicholson, “Debye shielding of a moving test charge in plasma,” *Journal of Plasma Physics*, vol. 25, no. 2, pp. 225–231, 1981.
- [14] P. K. Shukla and A. Mamun, *Introduction to dusty plasma physics*. CRC Press, 2015.

- [15] G. Emmert, R. Wieland, A. Mense, and J. Davidson, “Electric sheath and presheath in a collisionless, finite ion temperature plasma,” *The Physics of Fluids*, vol. 23, no. 4, pp. 803–812, 1980.
- [16] F. F. Chen and D. Arnush, “The floating potential of cylindrical langmuir probes,” *Physics of Plasmas*, vol. 8, no. 11, pp. 5051–5052, 2001.
- [17] F. F. Chen, “Langmuir probes in rf plasma: surprising validity of oml theory,” *Plasma Sources Science and Technology*, vol. 18, no. 3, p. 035012, 2009.
- [18] H. Hernandez, “Standard maxwell-boltzmann distribution: Definition and properties,” *ForsChem Research Reports*, vol. 2, 2017.
- [19] C. Cercignani, *Theory and application of the Boltzmann equation*. Scottish Academic Press, 1975.
- [20] C. R. Smith, “Bound states in a debye-hückel potential,” *Physical Review*, vol. 134, no. 5A, p. A1235, 1964.
- [21] C. Cui and J. Goree, “Fluctuations of the charge on a dust grain in a plasma,” *IEEE Transactions on plasma science*, vol. 22, no. 2, pp. 151–158, 1994.
- [22] Y. Tyshetskiy and S. Vladimirov, “Quantum-tunneling-enhanced charging of nanoparticles in plasmas,” *Physical Review E*, vol. 83, no. 4, p. 046406, 2011.
- [23] V. E. Fortov, A. P. Nefedov, V. M. Torchinsky, V. I. Molotkov, O. F. Petrov, A. A. Samarian, A. M. Lipaev, and A. G. Khrapak, “Crystalline structures of strongly coupled dusty plasmas in dc glow discharge strata,” *Physics Letters A*, vol. 229, no. 5, pp. 317–322, 1997.
- [24] D. S. Lea, “Motion of charged particles in em fields,” January 2007.
- [25] A. Ivlev, S. Zhdanov, S. Khrapak, and G. Morfill, “Kinetic approach for the ion drag force in a collisional plasma,” *Physical Review E*, vol. 71, no. 1, p. 016405, 2005.
- [26] T. Northrop, “Dusty plasmas,” *Physica Scripta*, vol. 45, no. 5, p. 475, 1992.
- [27] S. Khrapak, A. Ivlev, S. Zhdanov, and G. Morfill, “Hybrid approach to the ion drag force,” *Physics of plasmas*, vol. 12, no. 4, p. 042308, 2005.
- [28] J. D. Huba, “Nrl: Plasma formulary,” tech. rep., NAVAL RESEARCH LAB WASHINGTON DC BEAM PHYSICS BRANCH, 2004.
- [29] L. C. Andrews and L. C. Andrews, *Special functions of mathematics for engineers*. McGraw-Hill New York, 1992.
- [30] J. R. Roth, *Industrial Plasma Engineering: Volume 2-Applications to Nonthermal Plasma Processing*, vol. 2. CRC press, 2001.
- [31] D. Millar, “Ion currents, ion-neutral collisions and plasma transport phenomena,” *Australian Journal of Physics*, vol. 29, no. 4, pp. 249–262, 1976.

- [32] J. L. Synge, “Classical dynamics,” in *Principles of Classical Mechanics and Field Theory/Prinzipien der Klassischen Mechanik und Feldtheorie*, pp. 1–225, Springer, 1960.
- [33] A. D. Paro, *Horizontal Confinement of a Melamine Formaldehyde Dust Particle in an Argon Plasma*. PhD thesis, WORCESTER POLYTECHNIC INSTITUTE, 2012.
- [34] G. Ganguli, G. Joyce, and M. Lampe, “Phase transition in dusty plasmas,” in *Nonequilibrium Phenomena in Plasmas*, pp. 273–290, Springer, 2005.
- [35] J. Happel and H. Brenner, *Low Reynolds number hydrodynamics: with special applications to particulate media*, vol. 1. Springer Science & Business Media, 2012.
- [36] P. S. U. Professor J. M. Cimbala, “Drag on spheres,” 2012.
- [37] J. N. Reddy, *An introduction to the finite element method*, vol. 2. McGraw-Hill New York, 1993.
- [38] K. Seleznyova, M. Strugatsky, and J. Kliava, “Modelling the magnetic dipole,” *European Journal of Physics*, vol. 37, no. 2, p. 025203, 2016.
- [39] J. Vranjes, M. Kono, and M. Luna, “Charge exchange in fluid description of partially ionized plasmas,” *Monthly Notices of the Royal Astronomical Society*, vol. 455, no. 4, pp. 3901–3909, 2015.
- [40] B. Efron and R. J. Tibshirani, *An introduction to the bootstrap*. CRC press, 1994.
- [41] T. Acharya and P.-S. Tsai, “Computational foundations of image interpolation algorithms.,” *Ubiquity*, vol. 2007, no. October, pp. 4–1, 2007.
- [42] L. Matthews, K. Qiao, and T. Hyde, “Dynamics of a dust crystal with two different size dust species,” *Advances in Space Research*, vol. 38, no. 11, pp. 2564–2570, 2006.
- [43] S. D. Baalrud, “Influence of ion streaming instabilities on transport near plasma boundaries,” *Plasma Sources Science and Technology*, vol. 25, no. 2, p. 025008, 2016.